arXiv:1602.07150v3 [cond-mat.str-el] 17 Oct 2016

Topological phase transitions with SO(4) symmetry in (2+1)d interacting Dirac fermions

Xiao Yan Xu,[1] K. S. D. Beach,[2] Kai Sun,[3] F. F. Assaad,[4] and Zi Yang Meng[1]

[1]*Beijing National Laboratory for Condensed Matter Physics and Institute of Physics, Chinese Academy of Sciences, Beijing 100190, China*
[2]*Department of Physics and Astronomy, The University of Mississippi, University, Mississippi 38677, USA*
[3]*Department of Physics, University of Michigan, Ann Arbor, MI 48109, USA*
[4]*Institut für Theoretische Physik und Astrophysik, Universität Würzburg, 97074 Würzburg, Germany*

(Dated: September 5, 2016)

Interaction-driven topological phase transitions in Dirac semimetals are investigated by means of large-scale quantum Monte Carlo (QMC) simulations. The interaction among Dirac fermions is introduced by coupling them to Ising gauge variables that realize the quantum dynamics of the two-dimensional transverse field Ising model. The ground state phase diagram, in which the tuning parameters are the transverse field and the coupling between fermion and Ising spins, is determined. At weak and intermediate coupling, two different quantum phase transitions are observed, a second-order Ising quantum phase transition and a first-order topological phase transition between two topologically distinct Dirac semimetals. Interestingly, at this topological phase transition, the Dirac points smear out to form nodal lines in the Brillouin zone, and collective bosonic fluctuations comprised of the Dirac fermions with SO(4) symmetry are strongly enhanced. At strong coupling, these two phase boundaries merge into a first-order transition.

PACS numbers: 71.10.-w,71.10.Hf,75.40.Cx,75.40.Mg

Dirac fermions in (2+1)d emerge in a number of solid state systems such as graphene [1], surface states of 3D topological insulators [2], d-wave superconductors [3–5], and gapless spin liquids [6]. A parallel research track involves interaction-driven topological phase transitions in (2+1)d systems [7–18], which exhibit exotic quantum critical points and a break-down of the single-particle Green's function formalism for calculating the topological index [15, 16, 19]. An example is the phase transition in the (2+1)d non-linear σ model with a Θ term [17, 18]. In this context, an important question is what new physics would emerge if Dirac fermions and topological phase transitions were brought together via electronic interactions?

Timely developments in quantum Monte Carlo (QMC) techniques offer an opportunity to address this question: rather than simulating an explicit interaction between fermions, one can instead introduce bosonic fields that mediate fermion interaction. The key insight is that the form and behavior of these fields need not be limited to what would arise from a Hubbard-Stratonovich decomposition of explicit fermion interaction terms. One interesting direction is to endow the bosonic degrees of freedom with quantum dynamics of their own, such that they can be tuned through a quantum critical point (QCP). Examples of this approach include QMC studies of fermions in two dimensions coupled to nematic [20], antiferromagnetic [21–23] or Ising fluctuations [24, 25], which have revealed interesting features of metallic QCP as well as realizations of deconfined phases and phase transitions.

In this Letter, we consider a system of Dirac fermions on the square lattice, coupled to Ising gauge spins that decorate the nearest-neighbor links. Ordering of the Ising spins breaks the underlying C_{4v} symmetry and allows for anisotropic velocity renormalization of the Dirac points. We discover a first-order interaction-driven topological phase transition, at which collective bosonic fluctuations with SO(4) symmetry comprised of Dirac fermions are apparent. Across the transition, the bulk topological index, associated with the topological Dirac semimetal, flips its value and thereby shifts the momentum of the topologically protected edge states in the projected 1D Brillouin zone (BZ). Upon further increasing the transverse field and/or coupling, the second-order phase boundary of the Ising ordering merges with the topological phase transition into a first-order transition line.

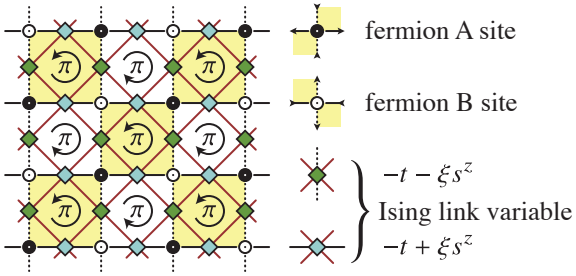

FIG. 1. (color online) Fermions on the π-flux square lattice, coupled to a transverse-field Ising model. Black and white circles represent sites in the A and B sublattices. Ising spins, denoted by filled diamonds, live on the links between adjacent fermionic sites and modify the corresponding hopping integral. The solid (dotted) lines indicate the positive (negative) character of the coupling between the Ising spins and the hopping. A magnetic flux of magnitude π runs through each plaquette. The arrows indicate the direction of the counter-circulating local currents.

Model and Method — We use sign-problem-free projector QMC [26–28] to simulate a model of fermions on the π-flux square lattice in which (i) the hopping is mediated by Ising spins positioned on the nearest-neighbor links and (ii) the Ising spins themselves interact via a two-dimensional transverse field Ising model (TFIM) on the dual lattice. Time rever-

sal symmetry of Eq. (1) guarantees positivity of the fermion determinant. The detailed description of our QMC implementation, including local-plus-global updates, is given in the supplemental material (SM) [29]. The model, illustrated in Fig. 1, has a Hamiltonian

$$H = \sum_{j,\delta} \left(-t + \mathrm{sgn}(\delta)\xi s^z_{j,j+\delta}\right)\left(c^\dagger_j c_{j+\delta}\, e^{i\frac{\pi}{4}\mathrm{sgn}(\delta)} + \mathrm{h.c.}\right) - J\sum_{\langle bb'\rangle} s^z_b s^z_{b'} - h\sum_b s^x_b. \quad (1)$$

Here, we have spin-1/2 fermions on the sites of a square lattice and an Ising spin $s^z_b = \pm 1$ on each bond with b being the bond index. $c^\dagger_j = \left(c^\dagger_{j\uparrow}, c^\dagger_{j\downarrow}\right)$ represents the fermionic creation operator for the site j. The dynamics of Ising variables is governed by a ferromagnetic ($J > 0$) TFIM. For the fermions, the nearest-neighbor hoppings are described by the first term in the Hamiltonian, where a sign factor $\mathrm{sgn}(\delta)$ is defined as $\mathrm{sgn}(\pm\hat{x}) = 1$ and $\mathrm{sgn}(\pm\hat{y}) = -1$. The phase factor $\frac{\pi}{4}\mathrm{sgn}(\delta)$ generates a π flux through each plaquette and the bare hopping strength $-t$ is modified by the Ising spin on the bond in proportion to the coupling strength ξ. Because $\mathrm{sgn}(\delta)$ takes the different sign for horizontal and vertical bonds, the spins modify the hoppings along the x and y directions oppositely, i.e., $s^z_b = +1$ increases the hopping strength for horizontal bonds, but decreases it for vertical bonds, and vice versa. This spin-fermion coupling relates the Z_2 Ising symmetry with the $\pi/2$ space rotational symmetry, i.e., an Ising ferromagnetic order will induce hopping anisotropy between x and y and thus results in an electronic nematic ordering [30].

In addition to the Ising and lattice point group symmetries, the fermionic degrees of freedom also preserve internal symmetries, independent of the ordering pattern of the Ising fields. $\mathrm{SU}_S(2)$ spin rotations, with generators S^α, and the particle-hole transformation, $P^{-1}c^\dagger_{i,\downarrow}P = (-1)^i c_{i,\downarrow}$, leave the Hamiltonian invariant. One can also define operators $\eta^\alpha = P^{-1}S^\alpha P$ that obey $\left[\eta^\alpha, S^\beta\right] = 0$. Hence, the full symmetry of the model is $\mathrm{SU}_S(2)\otimes\mathrm{SU}_\eta(2)\otimes\mathbb{Z}_{2,\mathrm{ph}}$ corresponding to the SO(4) symmetry of Ref. [31]. As a consequence of this enhanced symmetry, antiferromagnetic and superconducting states may coexist [32].

Results — We set $J = t = 1$ in the calculation. The QMC results are summarized in the ξ–h phase diagram of Fig. 2(a). At $\xi = 0$, the fermions and the Ising spins decouple. Because of the π flux, the fermions form a Dirac semimetal with Dirac points located at the X and Y points of the BZ. For the spin degrees of freedom, a 2D TFIM is recovered, where paramagnetic ($\langle s^z_b\rangle = 0$) and ferromagnetic ($\langle s^z_b\rangle \neq 0$) phases are separated by a quantum critical point at $h_c = 3.04(2)J$, consistent with previously reported values [33].

As we increase ξ, because couplings between Dirac fermions and Ising anisotropy is perturbatively irrelevant [3, 34, 35] [36], the second-order Ising phase transition shall remain with a renormalized critical h_c. This second-order phase boundary is indicated in Fig. 2 (a) as the solid black line. Upon further increasing ξ, new phenomena beyond the

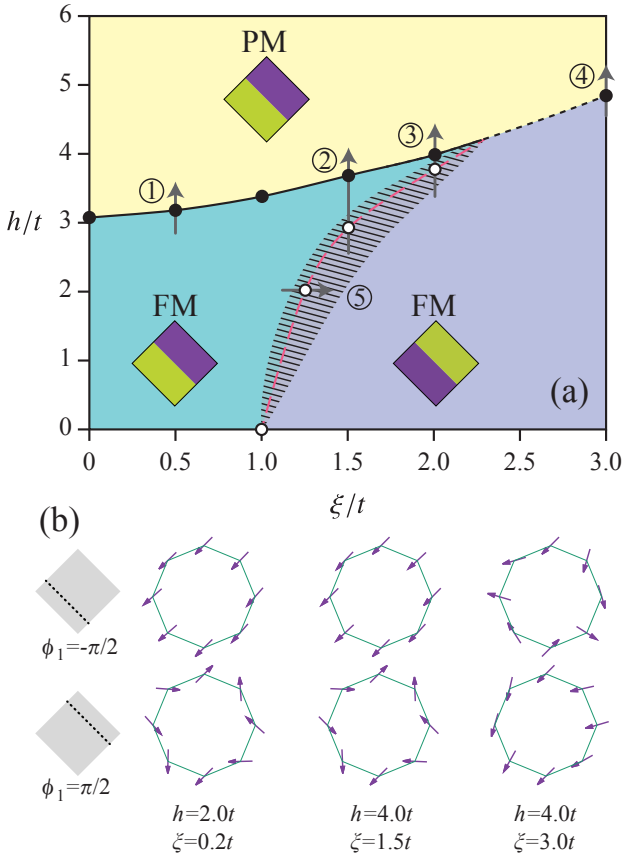

FIG. 2. (color online) (a) The ξ–h phase diagram. FM and PM indicate the ferromagnetic and paramagnetic Ising spin states. The insets stand for the 2d BZ of the system. Purple area is topologically nontrivial, with edge state in the projected 1d BZ, as shown in Fig. 3 (e) and (f). Green area is the topologically trivial part of BZ. Across the red dashed line, where the topological phase transition happens, the two areas of the BZ switch. The shaded area highlights the enhancement of collective SO(4) bosonic fluctuations in the fermion sector close to the red dashed line. The black solid line demarcates the FM-to-PM magnetic phase transition in Ising spins. Along paths ①, ②, and ③, this transition is still continuous, but along paths ④ and ⑤ it becomes first order. The magnetic correlations measured along paths ① to ④ are shown in Figs. 4 and 6. The correlation functions in the fermion sector along path ⑤ are shown in Fig. 5. (b) Topological index: the windings of the 2D vector $\mathbf{n}$ defined in the main text along $\phi_1 = \pm\pi/2$ loop for parameters: $h/t = 2, \xi/t = 0.2$, inside the left FM phase; $h/t = 4, \xi/t = 1.5$, inside PM phase; $h/t = 4, \xi/t = 3$, inside right FM phase.

TFIM arise. At $\xi > 1$, a new phase boundary emerge (dashed red line), at which strong singular behaviors in fermion bilinear are observed (the shaded area). As will be shown below, this new phase boundary is a first-order topological phase transition. At strong coupling ($\xi > 2.2$), the topological phase boundary (red dashed line) and the second-order Ising phase boundary (solid black line) merge together into a single first-order phase boundary (dashed back line).

To understand the topological phase transition, we first focus on the exactly solvable limit at $h = 0$ (the horizontal axis

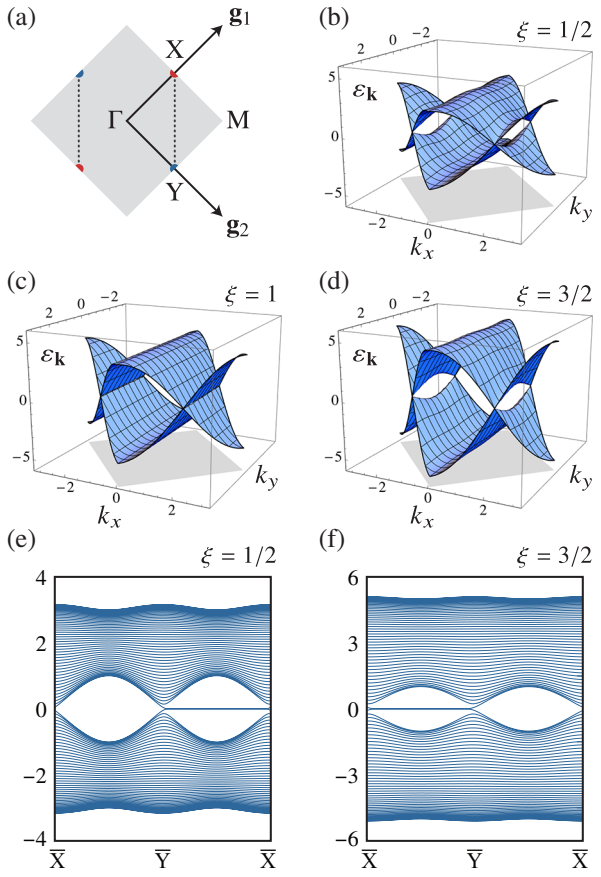

FIG. 3. (color online) (a) The BZ of the π-flux square lattice is the Wigner-Seitz cell constructed from the reciprocal lattice vectors $\mathbf{g}_1 = (\pi,\pi)$ and $\mathbf{g}_2 = (\pi,-\pi)$. Various high-symmetry points in the BZ are labeled by Γ, M, X, and Y. Two Dirac points are located at X $= (\pi/2,\pi/2)$ and Y $= (\pi/2,-\pi/2)$. The remaining panels shown the electronic dispersion $\varepsilon_{\mathbf{k}}$ at zero transverse field ($h = 0$) for coupling strengths (b) $\xi = 1/2$, (c) $\xi = 1$, and (d) $\xi = 3/2$. (e) and (f) Energy spectral with open boundaries plotted in the projected BZ $\bar{X} - \bar{Y} - \bar{X}$ at (e) $\xi = 1/2$ and (f) $\xi = 3/2$. The states at zero energy are topologically protected edge states, except for the Dirac points at $\bar{X}$ and $\bar{Y}$. Because the topological indices flip their values across the topological transtion as shown in Fig. 2, the edge states in (e) and (f) are located at different momentum points consistent with bulk topological index values.

of the phase diagram). In this limit, the Ising spins s_b^z commute with the Hamiltonian and thus have no quantum fluctuations. As a result, spins in the ground state must form a classical ferromagnetic spin configuration to minimize the energy $s_b^z = +1$ or $s_b^z = -1$. Without loss of generality, here we set $s_b^z = +1$ and then the system reduces into a free-fermion problem, whose band structure is shown in Fig. 3 (b)-(d) for different values of ξ. At finite ξ, as discussed above, the Ising ordering reduces the four-fold rotational symmetry down to two-fold (C_{4v} to C_{2v}). However, as long as $\xi \neq \pm 1$, the system remains a Dirac semimetal and the location of the Dirac points are pinned to X and Y by the C_{2v} point group symmetry. The reduction of the rotational symmetry is reflected by the anisotropy in Fermi velocity. Near a Dirac point (e.g. X), the linearized Hamiltonian is $H_X = 2(t-\xi)k_x\sigma_x + 2(t+\xi)k_y\sigma_y$, i.e., the Dirac point have different Fermi velocity along x and y. At $\xi = 1$, the velocity in one direction vanishes, and a nested fermi surface develops. This metallic state marks a topological phase transition between two topologically distinct Dirac semimetals.

To define the band topology for this 2D Dirac semimetal, it utilizes the idea of dimension reduction, in analogy to 3D Weyl semimetals [37–40] . In the momentum space, we can define the Hamiltonian for each momentum point $H(\phi_1,\phi_2)$, where a momentum point is labeled as $\mathbf{k} = \phi_1\mathbf{g_1}/2\pi + \phi_2\mathbf{g_2}/2\pi$ with $\mathbf{g}_1$ and $\mathbf{g}_2$ being the reciprocal lattice vectors shown in Fig. 3(a), and $-\pi < \phi_1 < \pi$ and $-\pi < \phi_2 < \pi$. For a fixed ϕ_1, i.e., one line in the BZ, the Hamiltonian, as a function of ϕ_2, can be treated as 1D system. For $\xi \neq \pm 1$ and $\phi_1 \neq 0$ or π, it is easy to verify that such a 1D system has a finite energy gap. Because of the chiral symmetry defined above, this gapped 1D system falls into the AIII class [41, 42] and thus support an integer valued topological index, i.e., a winding number. As required by the chiral symmetry, the Hamiltonian can be written as $H(\phi_1,\phi_2) = H_x(\phi_1,\phi_2)\sigma_x + H_y(\phi_1,\phi_2)\sigma_y$, where σ_x and σ_y are two of the Pauli matrices. A 2D unit vector can be defined as $\mathbf{n} = (H_x,H_y)/\sqrt{H_x^2+H_y^2}$ for $\xi \neq \pm 1$ and $\phi_1 \neq 0$ or π. For a fixed ϕ_1, as ϕ_2 increases from $-\pi$ to $+\pi$, this 2D vector winds $\mathscr{W}$ times around the unit circle. This winding number $\mathscr{W}$ is the topological index of this Dirac semimetal. For $0 < \xi < 1$, $\mathscr{W} = -1$ for $0 < \phi_1 < \pi$ and $\mathscr{W} = 0$ for $-\pi < \phi_1 < 0$. For $\xi > 1$, the topological index flips its value to $\mathscr{W} = 0$ for $0 < \phi_1 < \pi$ and $\mathscr{W} = -1$ for $-\pi < \phi_1 < 0$, i.e., $\xi = 1$ is a topological transition. To change a topological index, the bulk band gap must close, which results in the nodal lines shown in Fig. 3(c). The experimental signature for the band topology and topological transition lies in the edge states. As shown in Fig. 3(e–f), for $0 < \xi < 1$, the nontrivial bulk topological index for results in zero-energy energy states for projected momentum $0 < \phi_1 < \pi$. For $\xi > 1$, however, the zero-energy edge states shall shifts to momentum $-\pi < \phi_1 < 0$.

For $h \neq 0$, as shown in SM [29], the topological index can be defined utilizing an effective Hamiltonian, which is the inverse of the single-particle fermionic Green's functions at zero frequency [43]. Away from the shaded region in Fig. 2(a), the QMC simulations show finite single-particle gap for momentum points away from the Dirac points (X and Y), where the effective Hamiltonian is well-defined and gapped. We can then utilize this effective Hamiltonian to define the topological index away from the gapless momentum points, following the same procedure described above. In Fig. 2(b), we presented the winding number for $\phi_1 = \pm\pi/2$ at different values of ξ and h. Utilizing this method, find that the FM phase as two distinct topological semimetal phases (at small and large ξ). For the PM phase, the band topology coincides with the small ξ FM phase. As shown in SM [29], we further de-

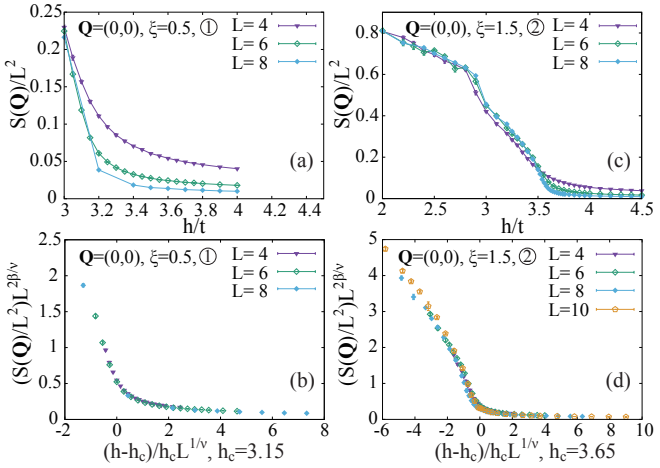

FIG. 4. (color online) (a) Correlation function $S(\mathbf{Q}=(0,0))$ of Ising spins along path ① for system sizes $L=4$, 6, and 8 at coupling $\xi=0.5$. (b) Rescaling of the correlation function data in (a) with (2+1)D Ising critical exponents. Note the high-quality data collapse. (c) $S(\mathbf{Q}=(0,0))$ of Ising spins along path ② at coupling $\xi=1.5$. There is a first-order transition between two FM states at $h\sim 2.8$, followed by a continuous FM-to-PM transition at $h_c=3.65$. (d) Collapse of the correlation function data in (c) close to h_c with (2+1)D Ising critical exponents.

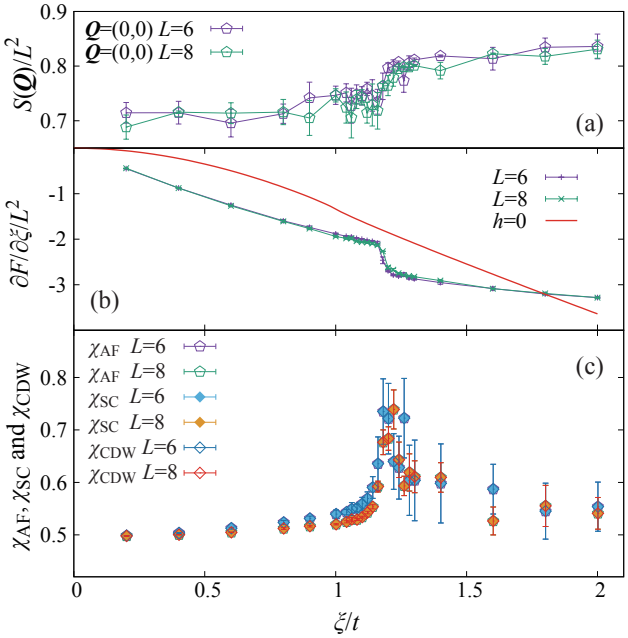

FIG. 5. (color online) Measurements along path ⑤. (a) Correlation function of the Ising spins. (b) The first derivative of the free energy with coupling strength. Here the $h=0$ case of $\partial F/\partial\xi$ is also plotted and the value has been scaled down by a factor of two for comparison in the same plot. The jump for $h=2.0$ case (data points with $L=6$ and 8) directly show a first order transition around $\xi/t\simeq 1.2$. (c) Fermionic spin-spin antiferromagnetic correlation functions $\chi_{\rm AF}$, on-site s-wave pairing correlations $\chi_{\rm SC}$, and CDW correlations $\chi_{\rm CDW}$. These functions are degenerate and greatly enhanced in the vicinity of the ξ/t value marked by the red dashed line in Fig. 2.

veloped a simplified method to compute the topological index. Instead of scanning a line in the momentum space, the topological index can be obtained by only focusing on the zero-frequency single-particle Green's function at momentum points $\phi_1=\pm\pi/2$ and $\phi_2=\pm\pi/2$.

Phase transitions— To better understand the phase transitions, we explore the phase diagram with several parameter scans. In what follows, we discuss QMC data along the five exemplary paths labeled ① through ⑤ in Fig. 2 (a).

For $\xi/t\lesssim 1$, the FM to PM phase transition is seemingly identical to that of the pure 2D TFIM, except for a small shift of the critical value of the transverse field. This statement is based on the evaluation of the correlation function of Ising spins, $S(\mathbf{Q})=\frac{1}{L^2}\sum_{bb'}\langle s^z_b s^z_{b'}\rangle e^{i\mathbf{Q}\cdot(\mathbf{r}_b-\mathbf{r}_{b'})}$ with b, b' running over all Ising spin sites and $\mathbf{Q}=(0,0)$. This data is shown in panels (a) and (b) of Fig. 4. The quality of the data collapse with (2+1)D Ising critical exponents is very good, which suggests that the FM to PM transition along path ① is still of (2+1)D Ising universality class [44]. Since the observed ferromagnetic ordering renormalizes the velocities, our result is consistent with the point of view that small velocity anisotropies that break Lorentz invariance are irrelevant [3, 34].

When the velocity renormalization becomes sufficiently large, it can trigger the topological phase transition. At $h=0$, the fermionic density of states diverge, as the result of the nesting Fermi surface inherent to particle-hole symmetric Hamiltonians, which results in divergent spin and charge susceptibilities. At a finite value of h, fluctuations of the Ising spins will provide an interaction between the fermionic degrees of freedom and, owing to the Stoner instability, will potentially trigger an instability, which leads to ordered state. Alternatively, a first-order transition can separate the two topologically different Dirac phases.

To investigate the above, we have computed $\frac{1}{L^2}\partial F/\partial\xi=\frac{1}{L^2}\sum_{j,\delta}\mathrm{sgn}(\delta)s^z_{j,j+\delta}\left\langle\left(c^\dagger_j c_{j+\delta}\ e^{i\frac{\pi}{4}\mathrm{sgn}(\delta)}+\mathrm{h.c.}\right)\right\rangle$, which is the derivative of the free-energy density F/L^2 over the control parameter of the transition ξ, along path ⑤. As shown in Fig. 5 (b), this derivative shows a clear jump at the transition point, which implies a first-order topological phase transition. The data for the Ising spin correlations in Fig. 5(a) is consistent with a first order transition, however within our error-bars, the discontinuity is hard to pin down.

We have also calculated the fermionic correlation functions along path ⑤, such as the fermionic spin-spin antiferromagnetic correlation functions $\chi_{\rm AF}=\frac{1}{L^2}\sum_{ij}(-1)^{i+j}\left(\langle s^z_i s^z_j\rangle-\langle s^z_i\rangle\langle s^z_j\rangle\right)$ with $s^z_i=\frac{1}{2}\left(c^\dagger_{i\uparrow}c_{i\uparrow}-c^\dagger_{i\downarrow}c_{i\downarrow}\right)$. Owing to the $\mathrm{SU}_S(2)\otimes\mathrm{SU}_\eta(2)\otimes Z_{2,\mathrm{ph}}$ symmetry of the model, this correlation function is degenerate with CDW correlations $\chi_{\rm CDW}=\frac{1}{L^2}\sum_{ij}(-1)^{i+j}\langle\eta^z_i\eta^z_j\rangle$, $\eta^z_i=(c^\dagger_{i\uparrow}c_{i\uparrow}+c^\dagger_{i\downarrow}c_{i\downarrow}-1)/2$ and with on-site s-wave pairing correlations $\chi_{\rm SC}=\frac{1}{2L^2}\sum_{ij}\langle\eta^+_i\eta^-_j\rangle$, $\eta^+_i=c^\dagger_{i\uparrow}c^\dagger_{i\downarrow}$. As shown in Fig. 5 (c), within numerical accuracy, the various correlation functions are indeed degenerate, and all develop a peak at $\xi/t\simeq 1.2$, which is consistent with

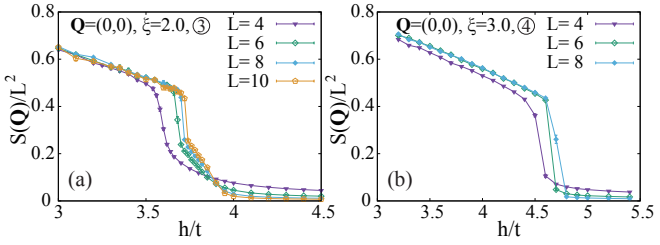

FIG. 6. (color online) (a) Correlation function $S(\mathbf{Q}=(0,0))$ of Ising spins along the path ③ for sizes $L=4$, 6, 8, and 10 with coupling $\xi=2.0$. As a function of h, there is a first-order transition between two FM states, following by a continuous transition between FM and PM states. (b) $S(\mathbf{Q}=(0,0))$ of Ising spins along path ④ with coupling $\xi=3.0$. There is a single first-order transition between FM and PM states.

the relation $\xi S(Q)/tL^2=1$ describing the divergence of the density of states at the mean-field level. Since there are no significant size effects between the considered lattice sizes, the data is consistent with the absence of long-range order and associated breaking of the SO(4) symmetry. We use a cross-hatched region in the Fig. 2 phase diagram to present an area where the SO(4) bosonic fluctuations are greatly enhanced. For the case of broken symmetry states, the coexistence of s-wave pairing and antiferromagnetism has been discussed in detail in Ref. [24, 32]. Note that at the value of h considered in Fig. 5 (deep inside FM state), the Ising spins are only weakly fluctuating. The QMC simulation dynamics are thus slow (see the discussion in Sec. S-II of SM [29]).

At larger values of h, fluctuations of the Ising spins become stronger. Along paths ② and especially ③ and ④, we see first-order transitions between the Dirac phases with different topological index. As illustrated along path ② in Fig. 4(c), as a function of growing values of h we first observe this first-order transition between the two FM states and then a (2+1)D Ising transition from FM to PM in the Ising spins, similar situation happens in Fig. 6(a). Further increase ξ, the Ising spins only develop a first-order transition from FM to PM states, as shown in Fig. 6(b).

Discussion and Conclusions — We have used an effective model of Dirac fermions, realized by the π-flux tight-binding model on the square lattice, coupled to a transverse Ising field in order to investigate the robustness of Dirac fermions to fluctuations that break the C_{4v} symmetry. At the mean-field level, where the Ising spins are either disordered or ferromagnetically ordered, the C_{4v} symmetry is broken down to C_{2v} in such a way that the positions of the Dirac nodes remain unchanged but the fermion velocities develop an anisotropy. Using unbiased QMC simulations, we show that the universality class of the Ising quantum phase transition remains in the (2+1)D Ising universality class, provided that the coupling between the Ising and fermion degrees of freedom is weak. This serves as a numerical proof that *small* velocity anisotropies in Dirac systems are irrelevant. At larger couplings, however, where the velocity is strongly renormalized, we observe enhanced spin and superconducting fluctuations around points in phase space where one of the velocities vanishes. The locking of antiferromagnetic correlations and s-wave superconductivity is a consequence of the SO(4) symmetry present in the model. At these points, the Berry phases of the Dirac cones interchange, and the transition turns out to be of first order.

Our model emphasizes fluctuations in velocity as opposed to fluctuations in the position of the Dirac points. It has some similarity to recent work reported in Ref. 20, and we can easily extend it to more complicated fermi surfaces. The flexibility of our numerical approach allows for arbitrary couplings between Ising spins and Dirac fermions such that velocity and Dirac point fluctuations can be investigated. Finally, we note that doping away from the half-filled case is possible since the time reversal symmetry, which permits sign-problem–free simulation, remains unbroken.

Acknowledgments — The authors thank E. Berg and I. Herbut for helpful discussions. XYX and ZYM are supported by the National Natural Science Foundation of China (NSFC Grant Nos. 11421092 and 11574359) and the National Thousand-Young-Talents Program of China. FFA is supported by the DFG under Grant FOR1807. KSDB and FFA gratefully acknowledge the hospitality of the Institute of Physics, Chinese Academy of Sciences. We thank the following institutions for allocation of CPU time: the Center for Quantum Simulation Sciences in the Institute of Physics, Chinese Academy of Sciences; the National Supercomputer Center in Tianjin; the John von Neumann Institute for Computing (NIC) for providing access to the supercomputer JURECA [45] at Jülich Supercomputing Centre (JSC); and the Gauss Centre for Supercomputing e.V. (www.gauss-centre.eu) for providing access to the GCS Supercomputer SuperMUC at Leibniz Supercomputing Centre (LRZ, www.lrz.de).

[1] K. S. Novoselov, A. K. Geim, S. V. Morozov, D. Jiang, Y. Zhang, S. V. Dubonos, I. V. Grigorieva, and A. A. Firsov, Science **306**, 666 (2004).
[2] Y. Xia, D. Qian, D. Hsieh, L. Wray, A. Pal, H. Lin, A. Bansil, D. Grauer, Y. S. Hor, R. J. Cava, and M. Z. Hasan, Nat Phys **5**, 398 (2009).
[3] M. Vojta, Y. Zhang, and S. Sachdev, Phys. Rev. Lett. **85**, 4940 (2000).
[4] E.-A. Kim, M. J. Lawler, P. Oreto, S. Sachdev, E. Fradkin, and S. A. Kivelson, Phys. Rev. B **77**, 184514 (2008).
[5] Y. Huh and S. Sachdev, Phys. Rev. B **78**, 064512 (2008).
[6] M. Hermele, T. Senthil, and M. P. A. Fisher, Phys. Rev. B **72**, 104404 (2005).
[7] K. Sun, H. Yao, E. Fradkin, and S. A. Kivelson, Phys. Rev. Lett. **103**, 046811 (2009).
[8] C. N. Varney, K. Sun, M. Rigol, and V. Galitski, Phys. Rev. B **82**, 115125 (2010).
[9] C. N. Varney, K. Sun, M. Rigol, and V. Galitski, Phys. Rev. B **84**, 241105 (2011).
[10] M. Hohenadler, T. C. Lang, and F. F. Assaad, Phys. Rev. Lett. **106**, 100403 (2011).
[11] M. Hohenadler, Z. Y. Meng, T. C. Lang, S. Wessel, A. Mura-

matsu, and F. F. Assaad, Phys. Rev. B **85**, 115132 (2012).
[12] T. C. Lang, A. M. Essin, V. Gurarie, and S. Wessel, Phys. Rev. B **87**, 205101 (2013).
[13] Y.-Z. You, Z. Bi, D. Mao, and C. Xu, Phys. Rev. B **93**, 125101 (2016).
[14] H.-Q. Wu, Y.-Y. He, C. Fang, Z. Y. Meng, and Z.-Y. Lu, Phys. Rev. Lett. **117**, 066403 (2016).
[15] Y.-Y. He, H.-Q. Wu, Z. Y. Meng, and Z.-Y. Lu, Phys. Rev. B **93**, 195163 (2016).
[16] Y.-Y. He, H.-Q. Wu, Z. Y. Meng, and Z.-Y. Lu, Phys. Rev. B **93**, 195164 (2016).
[17] K. Slagle, Y.-Z. You, and C. Xu, Phys. Rev. B **91**, 115121 (2015).
[18] Y.-Y. He, H.-Q. Wu, Y.-Z. You, C. Xu, Z. Y. Meng, and Z.-Y. Lu, Phys. Rev. B **93**, 115150 (2016).
[19] F. F. Assaad, M. Bercx, and M. Hohenadler, Phys. Rev. X **3**, 011015 (2013).
[20] Y. Schattner, S. Lederer, S. A. Kivelson, and E. Berg, Phys. Rev. X **6**, 031028 (2016).
[21] E. Berg, M. A. Metlitski, and S. Sachdev, Science **338**, 1606 (2012).
[22] Y. Schattner, M. H. Gerlach, S. Trebst, and E. Berg, Phys. Rev. Lett. **117**, 097002 (2016).
[23] M. H. Gerlach, Y. Schattner, E. Berg, and S. Trebst, arXiv:1609.08620 [cond-mat.str-el] (2016).
[24] F. F. Assaad and T. Grover, ArXiv e-prints (2016), arXiv:1607.03912 [cond-mat.str-el].
[25] S. Gazit, M. Randeria, and A. Vishwanath, ArXiv e-prints (2016), arXiv:1607.03892 [cond-mat.str-el].
[26] G. Sugiyama and S. Koonin, Annals of Physics **168**, 1 (1986).
[27] S. Sorella, S. Baroni, R. Car, and M. Parrinello, EPL (Europhysics Letters) **8**, 663 (1989).
[28] F. Assaad and H. Evertz, in *Computational Many-Particle Physics*, Lecture Notes in Physics, Vol. 739, edited by H. Fehske, R. Schneider, and A. Weiße (Springer Berlin Heidelberg, 2008) pp. 277–356.
[29] See Supplemental Material at http://link.aps.org/supplemental/xxx for additional details on the implementation of the QMC algorithm, the absence of a sign problem, and the local+global update scheme.
[30] S. A. Kivelson, E. Fradkin, and V. J. Emery, Nature **393**, 550 (1998).
[31] C. N. Yang and S. C. Zhang, Modern Physics Letters B **04**, 759 (1990).
[32] M. Feldbacher, F. F. Assaad, F. Hébert, and G. G. Batrouni, Phys. Rev. Lett. **91**, 056401 (2003).
[33] P. Pfeuty and R. J. Elliott, Journal of Physics C: Solid State Physics **4**, 2370 (1971).
[34] O. Vafek, Z. Tešanović, and M. Franz, Phys. Rev. Lett. **89**, 157003 (2002).
[35] L. Balents, M. P. A. Fisher, and C. Nayak, International Journal of Modern Physics B **12**, 1033 (1998).
[36] Because of symmetry, the Ising ordering in our model only modifies the Fermi velocity without changing the locations of the Dirac points, which implies that in the long-wavelength limit, the coupling between the Ising fields and fermion bilinears requires at least one spatial derivative and thus is irrelevant in strong analogy to case (C) in Ref. [3].
[37] X. Wan, A. M. Turner, A. Vishwanath, and S. Y. Savrasov, Phys. Rev. B **83**, 205101 (2011).
[38] H. Weng, R. Yu, X. Hu, X. Dai, and Z. Fang, Advances in Physics **64**, 227 (2015).
[39] A. A. Burkov, M. D. Hook, and L. Balents, Phys. Rev. B **84**, 235126 (2011).
[40] P. Hosur, S. A. Parameswaran, and A. Vishwanath, Phys. Rev. Lett. **108**, 046602 (2012).
[41] A. Kitaev, AIP Conference Proceedings **1134**, 22 (2009).
[42] A. P. Schnyder, S. Ryu, A. Furusaki, and A. W. W. Ludwig, Phys. Rev. B **78**, 195125 (2008).
[43] Z. Wang and S.-C. Zhang, Phys. Rev. X **2**, 031008 (2012).
[44] G. G. Batrouni and R. T. Scalettar, in *Ultracold Gases and Quantum Information*, Vol. 91 (Oxford University Press, Oxford, 2011) lecture Notes of the Les Houches Summer School in Singapore.
[45] Jülich Supercomputing Centre, Journal of large-scale research facilities **2**, A62 (2016).